Article

Not peer-reviewed version

# An Energy Management Strategy for Electrified Railway Smart Microgrid System Based on Integrated Empirical Mode Decomposition

Jingjing Ye , Minghao Sun , Kejian Song *

Posted Date: 18 December 2023

doi: 10.20944/preprints202312.1202.v1

Keywords: Hybrid energy storage system; Electric railway smart microgrid system; Integrated empirical mode decomposition; Two-stage energy distribution doi:10.20944/preprints202312.1202.v1

*Article*

# An Energy Management Strategy for Electrified Railway Smart Microgrid System Based on Integrated Empirical Mode Decomposition

**Jingjing Ye, Minghao Sun and Kejian Song ***

School of Electrical Engineering, Beijing Jiaotong University, Beijing, 100044, China; jjye@bjtu.edu.cn; 22121503@bjtu.edu.cn.; songkj@bjtu.edu.cn
* Correspondence: songkj@bjtu.edu.cn

**Abstract:** The integration of renewable energy and hybrid energy storage system (HESS) into electrified railways to build electric railway smart microgrid system (ERSMS) is beneficial for reducing fossil fuel consumption and minimizing energy waste. However, the fluctuations of renewable energy generation and traction load challenge the energy management effectiveness for such a complex system. In this work, an energy management strategy is proposed which firstly decomposes the renewable energy into low-frequency and high-frequency components by an integrated empirical mode decomposition (IEMD). Then, a two-stage energy distribution approach is utilized to appropriately distribute the energy flow among the ERSMS. Finally, the feasibility and effectiveness of the proposed solution are validated through case study.

**Keywords:** hybrid energy storage system; electric railway smart microgrid system; integrated empirical mode decomposition; two-stage energy distribution

## 1. Introduction

Nowadays, it has become a global consensus that we should fully utilize renewable energy sources due to concerns regarding energy security and environmental degradation. As a typical major energy consumer, the electrified railway system is with a strong demand for energy conservation [1]. Renewable energy sources, photovoltaic (PV), wind power (WP), etc., can be integrated with conventional traction power supply system (TPSS) which solely obtains electricity from the public grid powering the electrified railway, forming an electrified railway smart microgrid system (ERSMS) [2–4]. Apparently, the ERSMS is an energy saving and environmental-friendly option [5–9]. However, both traction load and renewable energy sources are highly stochastic and fluctuating. Potentially, this produces some power quality and transient disturbance issues to ERSMS operation. In addition, the regenerative braking energy (RBE) generated by locomotives will be injected to the overhead line, impacting the power flow of ERSMS as well [10,11]. Incorporating an energy storage system (ESS) into the ERSMS has become a common choice for power conditioning and RBE storage [12–15]. However, there are two main challenges for building a complex ERSMS containing an ESS: the first is to appropriately select energy storage media for matching the energy requirement of specific usage scenario; the second is to develop a high-performance energy management strategy (EMS) for distributing energy within the ERSMS, mitigating fluctuations and enhancing energy utilization efficiency.

There are a number of energy storage media, which are classified into two categories: high energy density and longer response time ones, represented by various batteries; high power density and short response time ones, represented by supercapacitors, flywheels [16]. Considering the substantial energy and power requirements of traction load and the fluctuation of renewable energy sources, a hybrid ESS (HESS) composing of batteries and supercapacitors is a reasonable solution for the ERSMS.

For EMS, the common method involves initially decomposing the power generated by renewable energy sources. This allows the HESS to store high-frequency components, while providing low-frequency or constant components to meet the load demand. The early used single-step methods are gradually abandoned [17–19]. Currently, the methods are time-frequency analysis-based ones such as Discrete Fourier Transform (DFT) [20], Discrete Wavelet Transform (DWT) [21] and Empirical Mode Decomposition (EMD) [22]. Both DFT and DWT are generally inappropriate for analyzing nonlinear and non-stationary signals [23]. Although the EMD is a better choice, it comes with mode mixing and disparate amplitudes issues in the intrinsic mode functions (IMFs) [24,25]. To tackle such issues, the complementary ensemble empirical mode decomposition with adaptive noise (CEEMDAN) was employed in [26], providing a resolution to the challenges encountered in EMD. Nevertheless, this method enhances the classification of IMFs using an improved empirical approach, there is room for further improve. After energy decomposition, it is essential to determine the energy distribution within the entire energy system. Recently, Liu et. al. developed a bi-level model of a railway traction substation energy management system for attaining optimal power reference and HESS size [27]. An EMS for ERSMS including PV and ESS has been proposed in [28], which enhances the overall economic efficiency of system operations. However, these approaches are restricted to a single renewable energy source or a single ESS, so that further research on EMS for ERSMS incorporating multiple renewable energy sources and HESS is required.

In view of the above, the present investigation aims to address the shortcomings of the EMD, as well as the research gaps in the complex energy distribution strategy for ERSMS. The main contribution and innovation of this work are as follows.

i) Combining the CEEMDAN and the grey relation analysis (GRA), an integrated empirical mode decomposition (IEMD) is proposed. The IEMD first divides the renewable energy into a series of IMFs, then classifies the IMFs to low frequency and high frequency components for distribution.

ii) On the basis of the supercapacitor absorbing high-frequency components and the HESS regulating low-frequency components of the renewable energy power, a two-stage distribution strategy is proposed for minimizing fluctuations of the renewable energy power in the ERSMS.

The remainder of this paper is organized as follows. Section 2 introduces the ERSMS configuration, including structure and operation modes. Section 3 introduces an integrated empirical mode decomposition method to decompose the renewable energy power. A two-stage energy distribution is proposed to distribute the power within the ERSMS in Section 4. Section 5 presents results based on designed case study. Finally, conclusions are drawn in Section 6.

## 2. ERSMS Configuration

### 2.1. Structure

The structure of a typical ERSMS is presented in Figure 1 which composes of four parts: a public grid, a TPSS, a renewable energy generation system and an HESS. In the TPSS a V/v connection traction transformer is installed for obtaining the power from the three-phase public grid supplying the traction load of the two single-phase catenary sections. A railway power conditioner (RPC) with single-phase ac-dc-ac topology is employed not only balancing the power between section a and section b [29], but also providing a dc link that a number of renewable energy generation and energy storage units can be connected to. So far, in this ERSMS the power exchanges among the four parts.

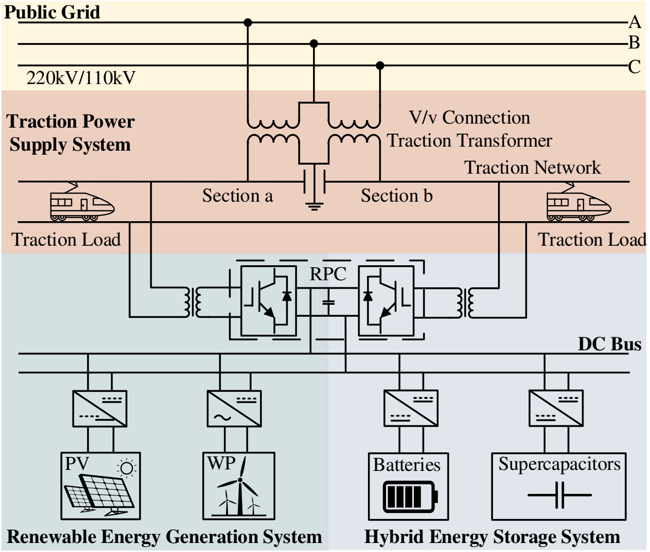

**Figure 1.** Structure of a typical ERSMS.

### 2.2. Operation modes

Different operation modes of the ERSMS can be classified based on the state of the traction load $P_L$ which is defined as the total power of the trains and the traction network loss of both section a and section b. By comparing $P_L$ with its traction state threshold value $P_{tra}$ and regenerative state threshold value $P_{reg}$, the following three ERSMS operation modes are defined.

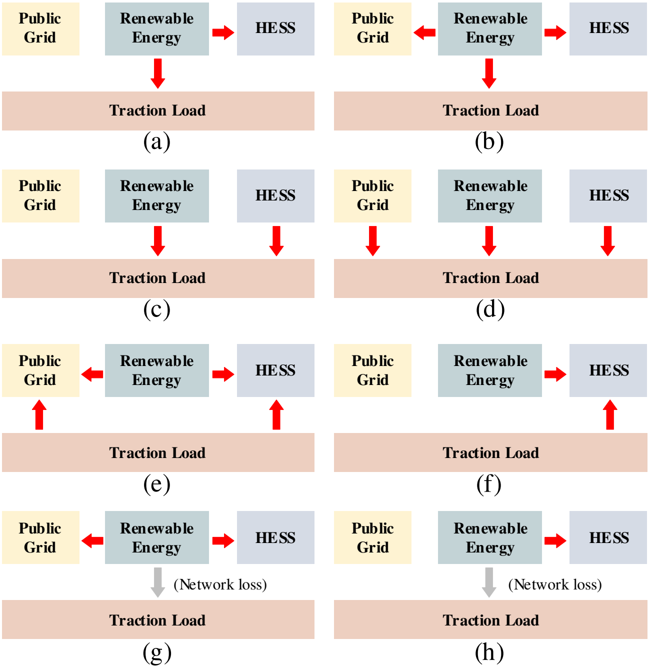

**Figure 2.** Operation modes of the ERSMS. (a) mode 1-1; (b) mode 1-2; (c) mode 1-3; (d) mode 1-4; (e) mode 2-1; (f) mode 2-2; (g) mode 3-1; (h) mode 3-2.

**Mode 1:** $P_L > P_{tra} > 0$

This is traction mode that traction power of the trains is more than regenerative braking power of the other trains. According to the absolute difference between the $P_L$ and the total renewable energy generation power $P_{ren}$, as well as the relative capacities of available charging and discharging power of the HESS, $P_{HESS\_Avail}$ and $P_{HESS\_Surp}$, this mode is further divided into four scenarios.

1. When $0 < P_{\text{ren}} - P_{\text{L}} \le P_{\text{HESS\_Avail}}$, the HESS is in charging state. In this situation, part of the $P_{\text{ren}}$ is used to meet the $P_{\text{L}}$, and all the rest are stored in the HESS, donated as $P_{\text{HESS}}$. The power flow relationship among the four parts of the ERSMS is demonstrated by Figure 2 (a) and Equation 1.

$$\begin{cases} P_{\text{HESS}} = P_{\text{ren}} - P_{\text{L}} \\ P_{\text{abd}} = 0 \end{cases} \tag{1}$$

2. When $P_{\text{HESS\_Avail}} < P_{\text{ren}} - P_{\text{L}}$ , the HESS is in charging state. After meeting the $P_{\text{L}}$ and fully charging the HESS, there is some excess power that cannot be utilized by the ERSMS. This part of power is named as abandoned power $P_{\text{abd}}$ which will be injected into the public grid or discarded. The power flow relationship of the ERSMS is demonstrated by Figure 2 and Equation 2.

$$\begin{cases} P_{\text{HESS}} = P_{\text{HESS\_Avail}} \\ P_{\text{abd}} = P_{\text{ren}} - P_{\text{L}} - P_{\text{HESS}} \end{cases} \tag{2}$$

3. When $0 < P_{\text{L}} - P_{\text{ren}} \le P_{\text{HESS\_Surp}}$ , the HESS is in discharging state. Under this condition, both $P_{\text{ren}}$ and $P_{\text{HESS}}$ support the $P_{\text{L}}$ together. The power flow relationship of the ERSMS is demonstrated by Figure 2 (c)and Equation 3.

$$\begin{cases} P_{\text{HESS}} = P_{\text{L}} - P_{\text{ren}} \\ P_{\text{abd}} = 0 \end{cases} \tag{3}$$

4. When $P_{\text{HESS\_Surp}} < P_{\text{L}} - P_{\text{ren}}$ , the HESS is in discharging state. Compared to previous condition, Pren and PHESS is insufficient for filling the PL. We have no choice but to purchase the lacking power from the public grid. The power flow relationship of the ERSMS is demonstrated in Figure 2 (d) and Equation 4.

$$\begin{cases} P_{\text{HESS}} = P_{\text{HESS\_Surp}} \\ P_{\text{abd}} = 0 \end{cases} \tag{4}$$

**Mode 2:** $P_{\text{L}} < P_{\text{reg}} < 0$

This is regenerative mode that traction power of the trains is less than regenerative braking power of the other trains. Apparently, the HESS is needed to be in charging state under this mode. By comparing the sum of $P_{\text{ren}}$ and $|P_{\text{L}}|$ with $P_{\text{HESS\_Avail}}$, this mode can be further divided into two scenarios.

When $P_{\text{ren}} + |P_{\text{L}}| > P_{\text{HESS\_Avail}}$, the HESS is in charging state. Although the HESS works at its maximum capacity, the $P_{\text{HESS}}$ cannot completely stores the $|P_{\text{L}}|$ (i.e., RBE) and $P_{\text{ren}}$. As a result, there is some $P_{\text{abd}}$ yet. The power flow relationship of the ERSMS is illustrated by Figure 2 (e) and Equation 5.

$$\begin{cases} P_{\text{HESS}} = P_{\text{HESS\_Avail}} \\ P_{\text{abd}} = P_{\text{ren}} + |P_{\text{L}}| - P_{\text{HESS}} \end{cases} \tag{5}$$

5. When $P_{\text{ren}} + |P_{\text{L}}| \le P_{\text{HESS\_Avail}}$, the HESS is a charging state. In this case, all the energy from the renewable energy generation and locomotive braking are stored into the HESS. The power flow of the ERSMS is illustrated by Figure 2 (f) and Equation 6.

$$\begin{cases} P_{\text{HESS}} = P_{\text{ren}} + |P_{\text{L}}| \\ P_{\text{abd}} = 0 \end{cases} \tag{6}$$

**Mode 3:** $P_{\text{reg}} < P_{\text{L}} < P_{\text{tra}}$

This is no-load mode regarding that there is no train load. The $P_{\text{L}}$ is only the open circuit loss of the traction network. Based on the comparison between $P_{\text{ren}}$ and $P_{\text{HESS\_Avail}}$, this mode is further divided into two scenarios.

doi:10.20944/preprints202312.1202.v1

When $P_{\text{ren}} > P_{\text{HESS\_Avail}}$, the HESS is in charging state. Part of $P_{\text{ren}}$ is absorbed by the maximum capacity of the HESS. The remaining of $P_{\text{ren}}$ becomes $P_{\text{abd}}$, excepting the little part addressing the network loss. The power flow relationship of the ERSMS is presented by Figure 2 (g) and Equation 7.

$$\begin{cases} P_{\text{HESS}} = P_{\text{HESS\_Avail}} \\ P_{\text{abd}} = P_{\text{ren}} - P_{\text{HESS}} - P_{\text{L}} \end{cases} \tag{7}$$

When $0 \le P_{\text{ren}} \le P_{\text{HESS\_Avail}}$, the HESS is in charging state. Excepting the little power for the network loss, renewable energy is fully stored in the HESS. The power flow relationship of the ERSMS is presented by Figure 2 (h) and Equation 8.

$$\begin{cases} P_{\text{HESS}} = P_{\text{ren}} - P_{\text{L}} \\ P_{\text{abd}} = 0 \end{cases} \tag{8}$$

As presented above, modes 1-1, 1-2, 1-3, 3-1, and 3-2 are fully energy self-sufficient; renewable energy may be abandoned in modes 1-2, 2-1, and 3-1; and purchasing power from the external grid is required in mode 1-4.

### *HESS Protection Strategy*

Typically, the state of charge (SOC) is the most critical factor for an energy storage system affecting the operating status and stability. For an HESS, five operation zones of the batteries and supercapacitors are defined according to their SOCs as shown in Figure 3: no charging/discharging zone, charge/discharge warning zone, and optimum working zone.

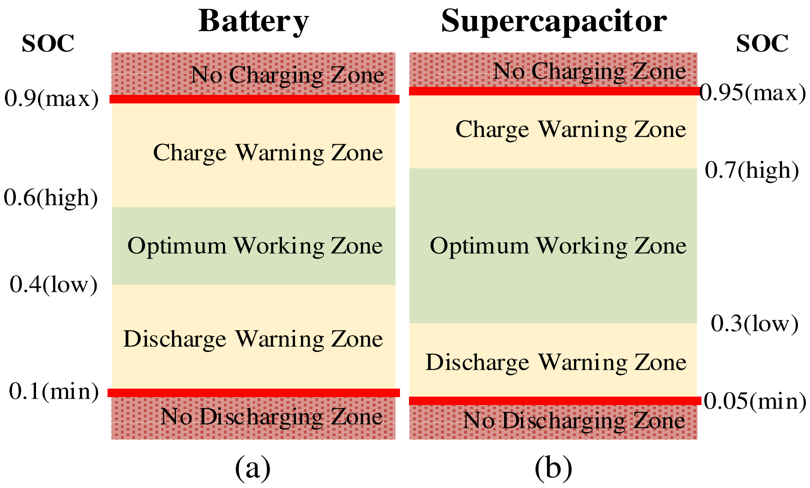

**Figure 3.** Operation zones corresponding to SOC: (a) battery; (b) supercapacitor.

When the SOC of battery or supercapacitor is outside the optimum working zone, the HESS cannot be charged or discharged at its maximum power capacity. Therefore, it is necessary to restrict the charging or discharging power according to the battery's or supercapacitor's remaining capacity. Based on the operation zone definition of Figure 3, a protection strategy is given as:

$$\begin{cases} P_{\text{c}}' = P_{\text{c}} \cdot \max\left\{0, \dfrac{SOC_{\max} - SOC}{SOC_{\max} - SOC_{\text{high}}}\right\} \\ P_{\text{d}}' = P_{\text{d}} \cdot \max\left\{0, \dfrac{SOC - SOC_{\min}}{SOC_{\text{low}} - SOC_{\min}}\right\} \end{cases} \tag{9}$$

where the subscripts c and d represent the charging and discharging states, respectively; $P_c'$ and $P_d'$ stand for the target charging and discharging power of the batteries or supercapacitors, respectively;

$P_\mathrm{c}$ and $P_\mathrm{d}$ are the target charging and discharging values without regard to restrict the charging or discharging power, respectively.

## 3. Integrated Empirical Mode Decomposition

Recognizing the shortcomings of unclear classification of the IMFs of conventional EMD methods, an IEMD is proposed combining a CEEMDAN decomposition and a GRA classification. First, apply the CEEMDAN to an original signal, i.e., the renewable energy power, by the following steps.

*Step* 1: Add the Gaussian white noise signal $\gamma^j(t)$ to $P_\mathrm{ren}$(t) which is the renewable energy generation power in time domain. The signal for the *j*-th is represented as $P_\mathrm{ren}^j(t) = P_\mathrm{ren}(t) + \varepsilon\gamma^j(t), j = 1, 2, \cdots, \mathrm{i}$ . The experimental signal $P_\mathrm{ren}^j(t)$ is decomposed by the EMD to obtain $IMF_1^j(t)$. The first IMF and the residual of the decomposition, donated as $P_\mathrm{IMF\text{-}1}(t)$ and $P_\mathrm{r1}(t)$ , are given as:

$$P_\mathrm{IMF\text{-}1}(t) = \frac{1}{I}\sum_{j=1}^{I} IMF_1^j(t) \tag{10}$$

$$P_\mathrm{r1}(t) = P_\mathrm{ren}(t) - P_\mathrm{IMF\text{-}1}(t) \tag{11}$$

*Step* 2: Add $\gamma^j(t)$ to the first residual $P_\mathrm{r1}(t)$, represented as $P_{r1}^j(t) = P_{r1}(t) + \varepsilon_1 E_1(\gamma^j(t)), j = 1, 2, \cdots, \mathrm{i}$. The $P_{r1}^j(t)$ are decomposed through the EMD as well obtaining their first-order components $IMF_2^j(t)$ . Similarly, the second IMF and residual are acquired:

$$P_\mathrm{IMF\text{-}2}(t) = \frac{1}{I}\sum_{j=1}^{I} IMF_2^j(t) \tag{12}$$

$$P_\mathrm{r2}(t) = P_\mathrm{r1}(t) - P_\mathrm{IMF\text{-}2}(t) \tag{13}$$

*Step* 3: Repeat the above process until the residual is monotony function and cannot be decomposed. At last, the original signal can be represented as the sum of a series IMFs as well as the residual.

$$P_\mathrm{ren}(t) = \sum_{k=1}^{K} P_\mathrm{IMF\text{-}k}(t) + P_\mathrm{r}(t) \tag{14}$$

After the decomposition above, some IMFs featuring fast fluctuation with lower magnitudes are defined as high-frequency IMFs (HF-IMFs); the others exhibiting slow fluctuation with higher magnitudes are defined as low-frequency IMFs (LF-IMFs). Although the IMFs can be simply classified by watching their shapes, in this work a GRA method is utilized to quantitatively classify them. Taking the use of the GRA, all the IMFs are classified by the following steps.

*Step* 1: The IMF and residual sequences are normalized by dividing their mean values.

$$P_\mathrm{IMF\text{-}i}^{'}(t) = \frac{P_\mathrm{IMF\text{-}i}(t)}{\overline{P}_\mathrm{IMF}}, i = 1, 2, ..., K \tag{15}$$

$$P_\mathrm{r}^{'}(t) = \frac{P_\mathrm{r}(t)}{\overline{P}_\mathrm{r}} \tag{16}$$

where, $\overline{P}_\mathrm{IMF}$ and $\overline{P}_\mathrm{r}$ represent the mean values of the IMFs and the residual, respectively.

*Step* 2: The first IMF $P_\mathrm{IMF\text{-}1}^{'}(t)$ is selected as the reference sequence in discrete time domain $P_\mathrm{tar}(t)$ , while the remaining IMFs and residual are designated as the comparison sequence $P_\mathrm{comp\text{-}i}(t)$ .

$$P_\mathrm{tar}(t) = P_\mathrm{IMF\text{-}1}^{'}(t) \tag{17}$$

$$P_{\text{comp-i}}(t)=\begin{cases}P'_{\text{IMF-i}}(t)\ ,i=2,3,\ldots,K\\ P'_{\text{r}}(t)\end{cases}\tag{18}$$

*Step* 3: Calculate the gray correlation coefficient $\xi_i$ and determine the grey correlation degree $r_i$.

$$\xi_i(t)=\frac{\min\limits_i\min\limits_t\left|P_{\text{tar}}(t)-P_{\text{comp-i}}(t)\right|}{\left|P_{\text{tar}}(t)-P_{\text{comp-i}}(t)\right|+\rho\max\limits_i\max\limits_t\left|P_{\text{tar}}(t)-P_{\text{comp-i}}(t)\right|}+\frac{\rho\max\limits_i\max\limits_t\left|P_{\text{tar}}(t)-P_{\text{comp-i}}(t)\right|}{\left|P_{\text{tar}}(t)-P_{\text{comp-i}}(t)\right|+\rho\max\limits_i\max\limits_t\left|P_{\text{tar}}(t)-P_{\text{comp-i}}(t)\right|}\tag{19}$$

$$r_i=\frac{1}{n}\sum\nolimits_{t=1}^{n}\xi_i(t),t=1,2,\ldots,n\tag{20}$$

where $\rho$ is the resolution coefficient (within the [0,1] interval; the value is usually 0.5).

*Step* 4: According to the values of $r_i$, the $P'_{\text{IMF-i}}(t)$ are sorted in ascending order. The ones with their $r$ values close to the $r_1$ are classified as HF-IMFs, the others with their $r$ values far from the $r_1$ are the LF-IMFs.

$$P_{\text{HF}}(t)=\sum_{i=1}^{u}P_{\text{IMF-i}}(t)\tag{21}$$

$$P_{\text{LF}}(t)=\sum_{i=1}^{v}P_{\text{IMF-i}}(t)+P_{\text{r}}(t)\tag{22}$$

where, $u$ and $v$ are the numbers of the HF-IMFs and the LF-IMFs, respectively.

## 4. Two-Stage Energy Distribution

So far, the decomposed renewable energy generation power should be distributed for utilization. The first distribution stage is based on that the supercapacitors absorb high-frequency renewable energy power $P_{\text{HF}}$(t) avoiding potential power quality and stability issues. The remaining low-frequency renewable energy power $P_{\text{LF}}$(t) is distributed by the second stage according to the operation modes as presented in subsection 2.2. The criterion is supplying the traction low by the renewable energy as much as possible. The two-stage distribution process is given in **Algorithm 1**.

After the initializing steps, the first stage starts from checking the SOC$_{\text{SC}}$. If it is within the normal range, the supercapacitors will be charged or discharged according to the $P_{\text{HF}}(k)$ under the given strategy. On the contrary, when SOC$_{\text{SC}}$ is out of the normal range, the $P_{\text{HF}}(k)$ will be discarded. Finally, refresh SOC$_{\text{HESS}}$ by SOC$_{\text{SC}}$.

The second stage starts from operation mode judgement. Then, if the SOC$_{\text{HESS}}$ is within a normal range, the HESS will balance the power flow among the ERSMS through charging or discharging under the given strategy. On the contrary, the SOC$_{\text{HESS}}$ out of the normal range, the HESS takes no action so that the traction load can just supplied by external grid.

**Algorithm 1:** The Two-Stage Energy Distribution

```
input  : $\mathrm{P}_{\mathrm{sc\_cmax}}$, $\mathrm{P}_{\mathrm{sc\_max}}$, $P_{\mathrm{HESS\_Surp}}$, $P_{\mathrm{HESS\_Avail}}$,
         $SOC_{\mathrm{sc\_max}}$, $SOC_{\mathrm{sc\_min}}$, $SOC_{\mathrm{HESS\_max}}$,
         $SOC_{\mathrm{HESS\_min}}$, $P_{\mathrm{HF}}(t)$, $P_{\mathrm{LF}}(t)$, $\mathrm{P}_{\mathrm{reg}}$, $\mathrm{P}_{\mathrm{tra}}$
output: $P_{\mathrm{HESS}}(t)$, $P_{\mathrm{abd}}(t)$
initial $SOC_{sc}(1) = 50\%$, $SOC_{bat}(1) = 50\%$;
for $k = 1; k \leq t; k++$ do
    ⊙HESS Power First distribution;
    if $SOC_{sc}(k) \in [SOC_{sc\_min}, SOC_{sc\_max}]$ then
        if $P_{\mathrm{HF}}(k) \geq 0$ then
            $P_{\mathrm{sc}}(k) = \min\{P_{\mathrm{HF}}(t), P_{\mathrm{sc\_cmax}}, P_{\mathrm{HESS\_Avail}}\}$;
            $P_{\mathrm{abd}}(k) = |P_{\mathrm{HF}}(k) - P_{\mathrm{sc}}(k)|$;
        end
        else
            $P_{\mathrm{sc}}(k) = \min\{P_{\mathrm{HF}}(t), P_{\mathrm{sc\_dmax}}, P_{\mathrm{HESS\_Surp}}\}$;
            $P_{\mathrm{abd}}(k) = |P_{\mathrm{HF}}(k) - P_{\mathrm{sc}}(k)|$;
        end
    end
    else
        $P_{\mathrm{sc}}(k) = 0, P_{\mathrm{abd}}(k) = P_{\mathrm{HF}}(t)$
    end
    $SOC_{\mathrm{sc}}(k) = P_{\mathrm{sc}}(k)/P_{\mathrm{sc\_max}}$
    $SOC_{\mathrm{HESS}}(k) = SOC_{\mathrm{sc}}(k) + SOC_{\mathrm{bat}}(k)$
    ⊙HESS Power Second distribution;
    if $P_{\mathrm{L}}(k) > P_{\mathrm{tra}}$ then
        if $SOC_{\mathrm{HESS}}(k) \in [SOC_{\mathrm{HESS\_min}}, SOC_{\mathrm{HESS\_max}}]$ then
            if $P_{\mathrm{L}}(k) \leq P_{\mathrm{LF}}(k)$ then
                $P_{\mathrm{HESS}}(k) = \min\{P_{\mathrm{LF}}(k) - P_{\mathrm{L}}(k), P_{\mathrm{HESS\_Avail}}\}$;
                  $P_{\mathrm{abd}}(k) = P_{\mathrm{LF}}(k) - P_{\mathrm{HESS}}(k) - P_{\mathrm{L}}(k)$;
            end
            else
                $P_{\mathrm{HESS}}(k) = \min\{P_{\mathrm{L}}(k) - P_{\mathrm{LF}}(k), P_{\mathrm{HESS\_Surp}}\}$;
                  $P_{\mathrm{abd}}(k) = 0$;
            end
        end
        else
            $P_{\mathrm{HESS}}(k) = 0$; $P_{\mathrm{abd}}(k) = P_{\mathrm{LF}}(k)$;
        end
    end
    else if $P_{\mathrm{L}}(k) < P_{\mathrm{reg}}(k)$ then
        if $SOC_{\mathrm{HESS}}(k) \in [SOC_{\mathrm{HESS\_min}}, SOC_{\mathrm{HESS\_max}}]$ then
            if $P_{\mathrm{LF}}(k) + |P_{\mathrm{L}}(k)| > P_{\mathrm{HESS\_Avail}}$ then
                $P_{\mathrm{HESS}}(k) = \min\{|P_{\mathrm{LF}}(k)| + P_{\mathrm{L}}(k), P_{\mathrm{HESS\_Avail}}\}$;
                  $P_{\mathrm{abd}}(k) = P_{\mathrm{LF}}(k) - P_{\mathrm{HESS}}(k)$;
            end
            else
                $P_{\mathrm{HESS}}(k) = \min\{|P_{\mathrm{LF}}(k)|, P_{\mathrm{HESS\_Avail}}\}$;
                  $P_{\mathrm{abd}}(k) = 0$;
            end
        end
        else
            $P_{\mathrm{HESS}}(k) = 0$; $P_{\mathrm{abd}}(k) = P_{\mathrm{LF}}(k)$;
        end
    end
    else
        if $SOC_{\mathrm{HESS}}(k) \in [SOC_{\mathrm{HESS\_min}}, SOC_{\mathrm{HESS\_max}}]$ then
            if $P_{\mathrm{LF}}(k) \geq P_{\mathrm{HESS\_Avail}}$ then
                $P_{\mathrm{HESS}}(k) = P_{\mathrm{HESS\_Avail}}$;
                $P_{\mathrm{abd}}(k) = P_{\mathrm{LF}}(k) - P_{\mathrm{HESS}} - P_{\mathrm{L}}(k)$;
            end
            else
                $P_{\mathrm{HESS}}(k) = P_{\mathrm{LF}}(k) - P_{\mathrm{L}}(k)$; $P_{\mathrm{abd}}(k) = 0$;
            end
        end
        else
            $P_{\mathrm{HESS}}(k) = 0$; $P_{\mathrm{abd}}(k) = P_{\mathrm{LF}}(k)$;
        end
    end
end
```

## 5. Results

### 5.1. Parameters

The active power of the traction load of a traction substation during a given period is obtained from traction calculation based on a train operation schedule, as shown in Figure 4. For easy discerning the results, a short part of this load is zoomed in for illustrating the energy management performance.

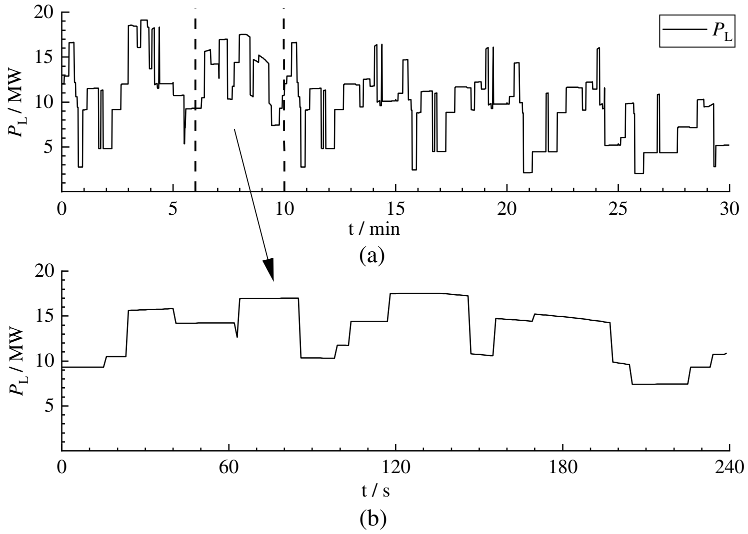

(a)

(b)

**Figure 4.** (**a**) Traction load power curve of a traction substation by traction calculation based on a train operation schedule; (**b**) zoom in a short part of the traction load power curve.

The renewable energy generation power under consideration is based on the weather data of a Chinese city. Figure 5 gives the wind power $P_{Wind}$, PV power $P_{PV}$ as well as their sum, i.e., the renewable energy power $P_{ren} = P_{Wind} + P_{PV}$, corresponding to the time of Figure 4. The average value and peak value of the wind power are 8.02 MW and 13.7 MW, respectively. The PV power fluctuates more severely with its average value of 6.92 MW and peak value of 25.38 MW. The total renewable energy power is with an average value of 14.94 MW and a peak value of 37.06 MW.

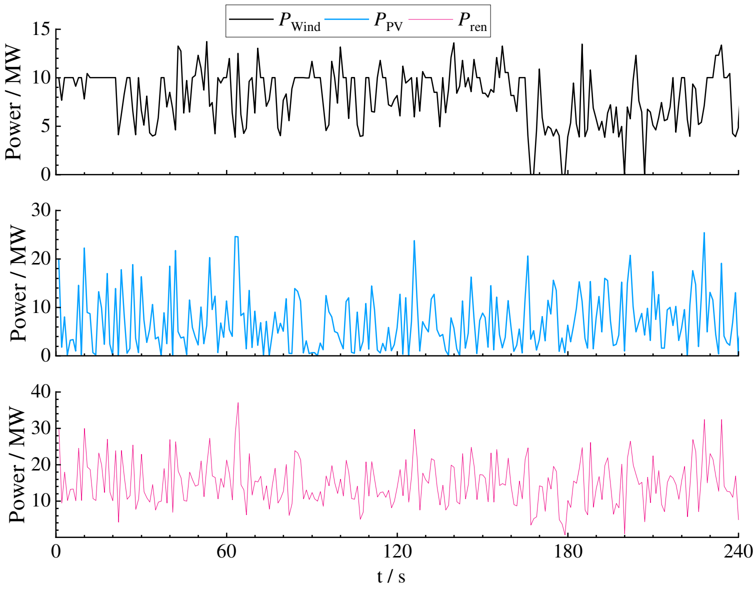

**Figure 5.** Typical renewable energy generation power.

Besides, the parameters of the HESS on concern are given in Table 1.

**Table 1.** HESS parameters.

| Parameter Name | Battery | Supercapacitor |
|---|---|---|
| Rated capacity (kW) | 20000 | 10000 |
| Maximum charging power (kW) | 11000 | 8500 |
| Maximum discharging power (kW) | 10500 | 8500 |
| Charging efficiency (%) | 90 | 95 |
| Discharging efficiency (%) | 90 | 95 |
| Maximum SOC (%) | 90 | 95 |
| Minimum SOC (%) | 10 | 5 |
| Current SOC (%) | 50 | 80 |

### *5.2. Case study*

The highly fluctuating renewable energy power shown in Figure 5 is decomposed and classified by the IEMD. Initially, the renewable energy power decomposition is conducted through the CEEMDAN procedure. As presented in Figure 6, seven IMFs and one residual (Res) of the renewable energy power are obtained. The IMFs and Res exhibit different shapes in terms of oscillation speed and magnitude.

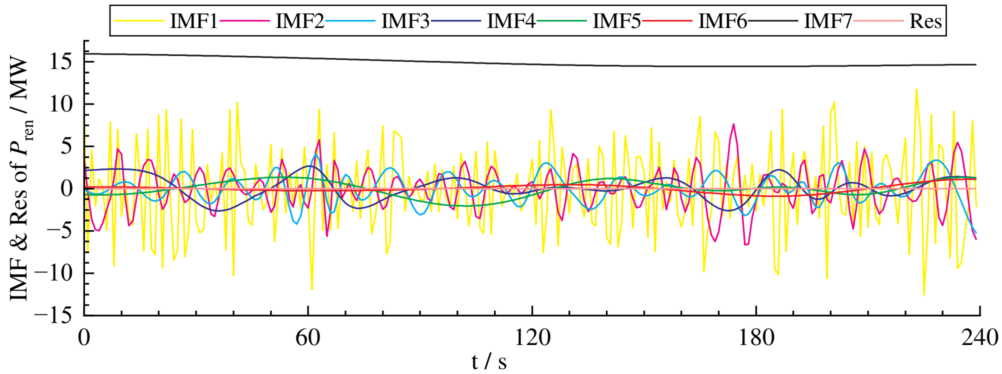

**Figure 6.** Decomposed IMFs and Res by CEEMDAN.

To divide these components more clearly, the IMFs are classified through the GRA procedure. According to Figure 6, the IMF1 (yellow line) is the most fluctuating component in both speed and magnitude angles. This means that the components correlate with this IMF1 are high-frequency ones, vice versa are low-frequency ones. Using IMF1 as the target sequence and the other six IMFs as comparison sequence, the grey correlation degree ($r$- value) can be obtained. Based on these $r$ values, a correlation heatmap of the IMFs is depicted as shown in Figure 7. The IMF2, IMF3, IMF4, IMF5 and IMF6 are with about 0.7 $r$ value to IMF1, i.e., high correlation. However, the $r$ value of the IMF7 is less than 0.4, i.e., not highly correlated with IMF1. This conclusion can be obtained by observing the color of the first column of the heatmap as well. Besides, the residual magnitude is extremely small, it is treated as one of the LF-IMFs. As a result, the $P_{ren}$ is divided into two sets, i.e., $P_{HF}(t)$ and $P_{LF}(t)$

$$P_{HF}(t) = \sum_{i=1}^{6} P_{IMF\text{-}i}(t) \tag{23}$$

$$P_{LF}(t) = P_{IMF\text{-}7}(t) + P_r(t) \tag{24}$$

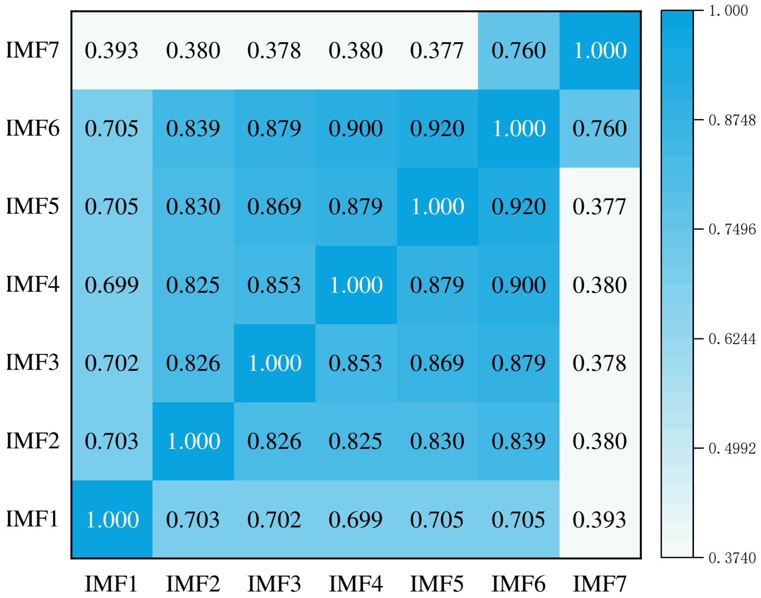

| | IMF1 | IMF2 | IMF3 | IMF4 | IMF5 | IMF6 | IMF7 |
|---|---|---|---|---|---|---|---|
| IMF7 | 0.393 | 0.380 | 0.378 | 0.380 | 0.377 | 0.760 | 1.000 |
| IMF6 | 0.705 | 0.839 | 0.879 | 0.900 | 0.920 | 1.000 | 0.760 |
| IMF5 | 0.705 | 0.830 | 0.869 | 0.879 | 1.000 | 0.920 | 0.377 |
| IMF4 | 0.699 | 0.825 | 0.853 | 1.000 | 0.879 | 0.900 | 0.380 |
| IMF3 | 0.702 | 0.826 | 1.000 | 0.853 | 0.869 | 0.879 | 0.378 |
| IMF2 | 0.703 | 1.000 | 0.826 | 0.825 | 0.830 | 0.839 | 0.380 |
| IMF1 | 1.000 | 0.703 | 0.702 | 0.699 | 0.705 | 0.705 | 0.393 |

**Figure 7.** The correlation heatmap of the IMFs.

So far, through the IEMD process, the decomposed LF-IMFs of renewable energy power are shown in Figure 8. Compared with the result of conventional EMD method, the $P_{LF}$ of the proposed IEMD shows much slower fluctuation with much smaller magnitude.

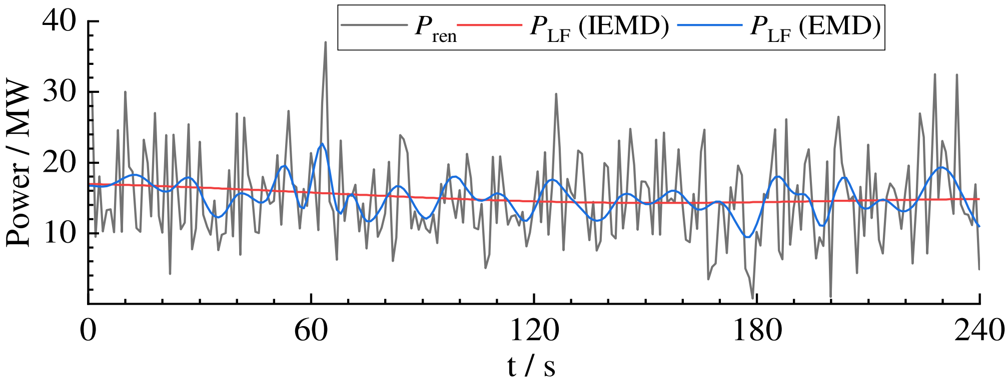

**Figure 8.** Decomposition results of $P_{LF}$ by proposed IEMD and conventional EMD.

At last, the decomposed renewable energy power is distributed by the two-stage method for utilization. The power decomposition results of both the proposed IEMD and conventional EMD are treated by the two-stage energy distribution, yielding the ERSMS supply result given by Figure 9. On the whole, in the ERSMS, the traction load is supplied by the renewable energy and the HESS as much as possible. After the two-stage energy distribution, the power flow of $P_{ren}$+$P_{HESS}$ by IEMD (blue line) becomes significant slower fluctuation compared to that of conventional EMD (pink line). This will benefit the lifespan of the HESS.

From the perspective of electricity consumption, owing to the two-stage energy distribution, most of the traction load are supplied by the $P_{ren}$+$P_{HESS}$ leading to a high energy self-sufficient rate. Furthermore, to the heavy load over 10 MW in Figure 9 (the parts upper than the dashed line), the $P_{ren}$ and $P_{HESS}$ cover nearly 89% of $P_L$ for proposed IEMD after the distribution (overlapped area of blue line and black line compared to the area of black line); while the counterpart of conventional EMD after the distribution is less than 83% (overlapped area of pink line and black line compared to the area of black line).

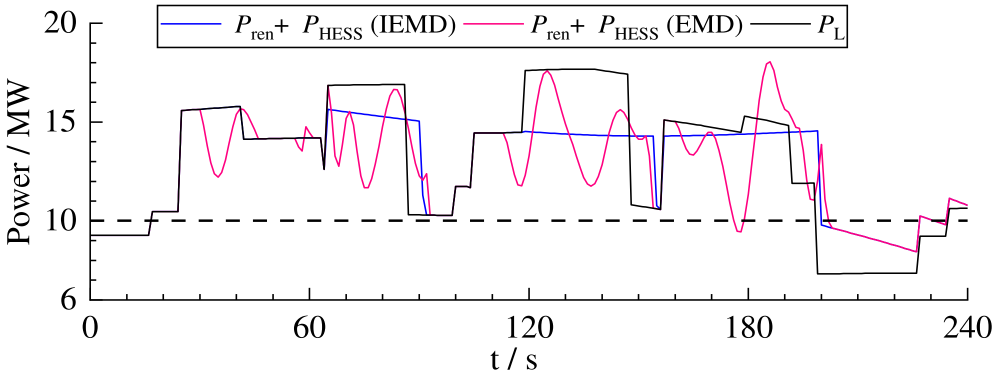

**Figure 9.** ERSMS supply results after the two-stage energy distribution based on proposed IEMD and conventional EMD.

## 6. Conclusion

This work proposed an energy management strategy for the integration of renewable energy and HESS in electrified railways. This strategy incorporates an IEMD process to the renewable energy generation power and a two-stage energy distribution for the energy flow among the ERSMS. By the IEMD, the severely fluctuating renewable energy generation power is divided into high-frequency and low-frequency parts. Through the two-stage energy distribution, the former is absorbed by the supercapacitors to the best of $SOC_{SC}$ ability, and the later is used by the traction load as much as possible based on HESS operation. The case study validates that the proposed method provides superior energy utilization performance than convention method by means of power fluctuation and electricity consumption.

**Author Contributions:** Conceptualization, J.Y. and M.S.; methodology, J.Y. and M.S.; validation, M.S. and K.S.; formal analysis, M.S. and K.S.; data curation, M.S.; writing—original draft preparation, M.S.; writing— review and editing, M.S., J.Y. and K.S.; supervision, J.Y. and K.S.; funding acquisition, J.Y. and K.S. All authors have read and agreed to the published version of the manuscript.

**Funding:** This work was supported by the Fundamental Research Funds for the Central Universities under Grant 2021CZ103.

**Institutional Review Board Statement:** Not applicable.

**Informed Consent Statement:** Not applicable.

**Data Availability Statement:** Not applicable.

**Conflicts of Interest:** The authors declare no conflict of interest.

## References

1. Douglas, H.; Roberts, C.; Hillmansen, S.; Schmid, F. An Assessment of Available Measures to Reduce Traction Energy Use in Railway Networks. Energy Conversion and Management 2015, 1149–1165, doi:10.1016/j.enconman.2015.10.053.
2. Brenna, M.; Foiadelli, F.; Kaleybar, H.J. The Evolution of Railway Power Supply Systems Toward Smart Microgrids: The Concept of the Energy Hub and Integration of Distributed Energy Resources. IEEE Electrification Magazine 2020, 12–23, doi:10.1109/mele.2019.2962886.
3. Pilo de la Fuente, E.; Mazumder, S.K.; Franco, I.G. Railway Electrical Smart Grids: An Introduction to next-Generation Railway Power Systems and Their Operation. IEEE Electrification Magazine 2014, 49–55, doi:10.1109/mele.2014.2338411.
4. Brenna, M.; Foiadelli, F.; Kaleybar, H.J.; Fazel, S.S. Smart Electric Railway Substation Using Local Energy Hub Based Multi-Port Railway Power Flow Controller. In Proceedings of the 2019 IEEE Vehicle Power and Propulsion Conference (VPPC); October 2019.
5. D'Arco, S.; Piegari, L.; Tricoli, P. Comparative Analysis of Topologies to Integrate Photovoltaic Sources in the Feeder Stations of AC Railways. IEEE Transactions on Transportation Electrification 2018, 951–960, doi:10.1109/tte.2018.2867279.

6. Hernandez, J.C.; Sutil, F.S. Electric Vehicle Charging Stations Feeded by Renewable: PV and Train Regenerative Braking. IEEE Latin America Transactions 2016, 3262–3269, doi:10.1109/tla.2016.7587629.
7. Zhu, X.; Hu, H.; Tao, H.; He, Z. Stability Analysis of PV Plant-Tied MVdc Railway Electrification System. IEEE Transactions on Transportation Electrification 2019, 311–323, doi:10.1109/tte.2019.2900857.
8. Aguado, J.A.; Sanchez Racero, A.J.; de la Torre, S. Optimal Operation of Electric Railways With Renewable Energy and Electric Storage Systems. IEEE Transactions on Smart Grid 2018, 993–1001, doi:10.1109/tsg.2016.2574200.
9. Boudoudouh, S.; Maaroufi, M. Renewable Energy Sources Integration and Control in Railway Microgrid. IEEE Transactions on Industry Applications 2019, 2045–2052, doi:10.1109/tia.2018.2878143.
10. Wang, Y.; Chen, M.; Guo, L.; Luo, J. Flexible Traction Power System Adopting Energy Optimisation Controller for AC-fed Railway. Electronics Letters 2017, 554–556, doi:10.1049/el.2017.0470.
11. Lu, Q.; He, B.; Wu, M.; Zhang, Z.; Luo, J.; Zhang, Y.; He, R.; Wang, K. Establishment and Analysis of Energy Consumption Model of Heavy-Haul Train on Large Long Slope. Energies 2018, 965, doi:10.3390/en11040965.
12. Cui, G.; Luo, L.; Liang, C.; Hu, S.; Li, Y.; Cao, Y.; Xie, B.; Xu, J.; Zhang, Z.; Liu, Y.; et al. Supercapacitor Integrated Railway Static Power Conditioner for Regenerative Braking Energy Recycling and Power Quality Improvement of High-Speed Railway System. IEEE Transactions on Transportation Electrification 2019, 702–714, doi:10.1109/tte.2019.2936686.
13. Gao, Z.; Lu, Q.; Wang, C.; Fu, J.; He, B. Energy-Storage-Based Smart Electrical Infrastructure and Regenerative Braking Energy Management in AC-Fed Railways with Neutral Zones. Energies 2019, 4053, doi:10.3390/en12214053.
14. Lu, Q.; Gao, Z.; He, B.; Che, C.; Wang, C. Centralized-Decentralized Control for Regenerative Braking Energy Utilization and Power Quality Improvement in Modified AC-Fed Railways. Energies 2020, 2582, doi:10.3390/en13102582.
15. Ma, F.; Wang, X.; Deng, L.; Zhu, Z.; Xu, Q.; Xie, N. Multiport Railway Power Conditioner and Its Management Control Strategy With Renewable Energy Access. IEEE Journal of Emerging and Selected Topics in Power Electronics 2020, 1405–1418, doi:10.1109/jestpe.2019.2899138.
16. Li, W.; Joos, G. A Power Electronic Interface for a Battery Supercapacitor Hybrid Energy Storage System for Wind Applications. In Proceedings of the 2008 IEEE Power Electronics Specialists Conference; June 2008.
17. Han, X.; Chen, F.; Cui, X.; Li, Y.; Li, X. A Power Smoothing Control Strategy and Optimized Allocation of Battery Capacity Based on Hybrid Storage Energy Technology. Energies 2012, 1593–1612, doi:10.3390/en5051593.
18. Li, X. Fuzzy Adaptive Kalman Filter for Wind Power Output Smoothing with Battery Energy Storage System. IET Renewable Power Generation 2012, 340–347, doi:10.1049/iet-rpg.2011.0177.
19. Howlader, A.M.; Matayoshi, H.; Senjyu, T. A Robust H∞ Controller Based Gain-Scheduled Approach for the Power Smoothing of Wind Turbine Generator with a Battery Energy Storage System. Electric Power Components and Systems 2015, 2156–2167, doi:10.1080/15325008.2015.1076089.
20. Makarov, Y.V.; Du, P.; Kintner-Meyer, M.C.W.; Jin, C.; Illian, H.F. Sizing Energy Storage to Accommodate High Penetration of Variable Energy Resources. IEEE Transactions on Sustainable Energy 2012, 34–40, doi:10.1109/tste.2011.2164101.
21. Jiang, Q.; Hong, H. Wavelet-Based Capacity Configuration and Coordinated Control of Hybrid Energy Storage System for Smoothing Out Wind Power Fluctuations. IEEE Transactions on Power Systems 2013, 1363–1372, doi:10.1109/tpwrs.2012.2212252.
22. Yuan, Y.; Sun, C.; Li, M.; Choi, S.S.; Li, Q. Determination of Optimal Supercapacitor-Lead-Acid Battery Energy Storage Capacity for Smoothing Wind Power Using Empirical Mode Decomposition and Neural Network. Electric Power Systems Research 2015, 323–331, doi:10.1016/j.epsr.2015.06.015.
23. Huang, N.E.; Shen, Z.; Long, S.R.; Wu, M.C.; Shih, H.H.; Zheng, Q.; Yen, N.-C.; Tung, C.C.; Liu, H.H. The Empirical Mode Decomposition and the Hilbert Spectrum for Nonlinear and Non-Stationary Time Series Analysis. Proceedings of the Royal Society of London. Series A: Mathematical, Physical and Engineering Sciences 1998, 903–995, doi:10.1098/rspa.1998.0193.
24. WU, Z.; HUANG, N.E. ENSEMBLE EMPIRICAL MODE DECOMPOSITION: A NOISE-ASSISTED DATA ANALYSIS METHOD. Advances in Adaptive Data Analysis 2009, 1–41, doi:10.1142/s1793536909000047.
25. Ren, Y.; Suganthan, P.N.; Srikanth, N. A Comparative Study of Empirical Mode Decomposition-Based Short-Term Wind Speed Forecasting Methods. IEEE Transactions on Sustainable Energy 2015, 236–244, doi:10.1109/tste.2014.2365580.

26. Li, M.; Li, Y.; Choi, S.S. Dispatch Planning of a Wide-Area Wind Power-Energy Storage Scheme Based on Ensemble Empirical Mode Decomposition Technique. IEEE Transactions on Sustainable Energy 2021, 1275–1288, doi:10.1109/tste.2020.3042385.
27. Liu, P.; Lai, J.; Chen, T.; Zeng, X.; Cheng, Y. Coordination Control Strategy of Co-Phase Traction Power Supply System Integrated with Hybrid Energy Storage Systems. In Proceedings of the 2022 5th International Conference on Energy, Electrical and Power Engineering (CEEPE); April 2022.
28. Li, X.; Zhu, C.; Liu, Y. Traction Power Supply System of China High-Speed Railway under Low-Carbon Target: Form Evolution and Operation Control.
29. Zhong, Z.; Zhang, Y.; Shen, H.; Li, X. Optimal Planning of Distributed Photovoltaic Generation for the Traction Power Supply System of High-Speed Railway. Journal of Cleaner Production 2020, 121394, doi:10.1016/j.jclepro.2020.121394.